PHYSICAL REVIEW B **92**, 174104 (2015)

Molecular dynamics simulation of subpicosecond double-pulse laser ablation of metals

Mikhail E. Povarnitsyn,[1] Vladimir B. Fokin,[1] Pavel R. Levashov,[1,2] and Tatiana E. Itina[3]
[1]*Joint Institute for High Temperatures RAS, Izhorskaya 13 Bldg 2, Moscow 125412, Russia*
[2]*Tomsk State University, 36 Lenin Prospekt, Tomsk 634050, Russia*
[3]*Laboratoire Hubert Curien, UMR CNRS 5516/Université de Lyon, Bât. F, 18 rue du Prof. Benoit Lauras, 42000 Saint-Etienne, France*

(Received 29 June 2015; revised manuscript received 1 September 2015; published 6 November 2015)

Subpicosecond double-pulse laser ablation of metals is simulated using a hybrid model that combines classical molecular dynamics and an energy equation for free electrons. The key advantage of our model is the usage of the Helmholtz wave equation for the description of the laser energy absorption. Applied together with the wide-range coefficients of optical and transport properties of the electron subsystem, the model gives the possibility to correctly describe the second pulse absorption on an arbitrary profile of the nascent plasma plume produced by the first pulse. We show that the integral absorption of the second pulse drastically increases with the delay between pulses, which varies in the simulation from 0 to 200 ps. As a result, the electron temperature in the plume increases up to three times with the delay variation from 0 to 200 ps. Thus the results of simulation resemble the previous experimental observations of the luminosity increase in the double-pulse irradiation for the delay interval from 100 to 200 ps. Besides, we bring to light two mechanisms of suppression of ablation responsible for the monotonic decrease of the ablation crater depth when the delay between pulses increases.

DOI: 10.1103/PhysRevB.92.174104 PACS number(s): 79.20.Eb, 64.60.Q−, 64.70.D−, 68.03.Fg

I. INTRODUCTION

Ultrashort subpicosecond double-pulse (DP) laser ablation of solids is used for a precise treatment of materials, to increase the spectral line intensities in laser-induced breakdown spectroscopy (LIBS) [1–4], for investigation of DP plume dynamics [5], optimization of the nanoparticle size distribution in vacuum [6,7] and liquids [8,9], and modification of optical properties [10,11]. During the last decade, the numerical modeling of ultrashort laser ablation of metals was focused on understanding the basic mechanisms responsible for the process of ablation [12,13] and dynamics of laser-irradiated nanoparticles [14,15]. In addition, efforts were aimed at optimizing the temporal laser pulse shape [16], the hydrodynamic simulation of a single pulse (SP) [17,18] and DP laser ablation [19,20], molecular dynamics (MD) simulation of SP [21–25] and DP laser ablation [26], as well as the study of ablation efficiency of a target wetted by a thin liquid film [27].

It is known that the absorption of laser energy in the optical range by polished metals is typically on the order of 10% at room temperature, and the rest of energy is reflected from the target surface. Thus the absorption of a subpicosecond SP can be approximated by an effective absorption coefficient that defines the energy distribution inside the skin layer of a metallic target. At the same time, a careful simulation of either multiple femtosecond interactions or even of an SP nanosecond laser ablation requires more sophisticated models. In particular, these models should account for laser energy absorption in an extended plume with a strongly nonhomogeneous distribution of thermodynamic parameters.

An atomistic simulation seems to be a very effective tool in the investigation of laser ablation since it allows to consider fluctuations of thermodynamic parameters on nanoscales, defects of atomic structure, kinetic processes of metastable phase nucleation, lattice overheating, evaporation and condensation as well as kinetics of homogeneous and heterogeneous melting and solidification. Difficulties in the application of this method to the simulation of laser-mater interaction arise when one needs to take into account the dynamics of an electron subsystem with a temperature higher than that of the ionic subsystem. In many early investigations, this nonequilibrium state was described by the continual two-temperature model (TTM) [28,29]. Ivanov and Zhigilei proposed an approach that accounts for the conduction band (CB) electrons in this two-temperature case [22] combining the MD method and the TTM model. In their model, the simulation of the SP laser energy absorption was based on the Beer's law that allows to consider only relatively weak laser pulses. Improvements of this approach [22] in successive works include the introduction of an electron temperature to the MD potential [30] as well as the inclusion of the blast force of delocalized electrons to the MD equations [24,31]. By using such modifications, however, it is hard to meet the energy conservation law, [32] and they are not suitable for the DP laser ablation considered here. The key physical factors in the last case involve the complex absorption of the laser radiation both in the skin layer and in the extended region of the subcritical plasma, wide-range models of electron thermodynamics, electron thermal conductivity, and electron-phonon/ion coupling, and the interaction of shock and rarefaction waves generated by both pulses.

To improve our understanding of the basic mechanisms of the DP laser ablation of metals, we develop a hybrid model that is based on the approach described in Ref. [22]. Then, we extend the model by a procedure of calculation of the laser energy absorption using the solution to the Helmholtz wave equation for each pulse. The dielectric function as well as the electron-phonon/ion coupling coefficient and the electron thermal conduction coefficient have a wide-range form described in detail in our previous paper [33].

The article is organized as follows. In Sec. II, we present the details of our hybrid MD-TTM model. Section III deals with the discussion of the results of the study that are summarized in Sec. IV.

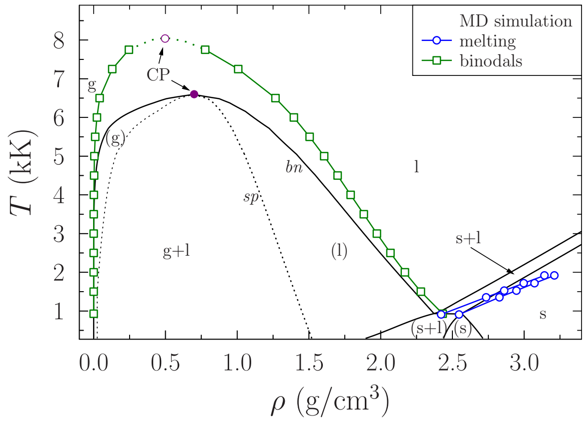

FIG. 1. (Color online) Phase diagrams of aluminum. EOS phase states are g: stable gas, l: stable liquid, s: stable solid, l+s: stable melting, g+l: liquid-gas mixture, (g): metastable gas, (l): metastable liquid, (l+s): metastable melting, (s): metastable solid, CP: critical point, *bn*: binodal, and *sp*: spinodal. Direct MD two-phase calculations: solid (green) lines with empty (green) squares show MD binodals, solid (blue) lines with empty (blue) circles show the MD melting region.

II. MOLECULAR DYNAMICS TWO-TEMPERATURE MODEL

In the MD method, the dynamics of the atomic subsystem is determined by an interatomic potential and boundary conditions. For metals, an embedded atom model (EAM) [34] is often used that accounts for both a pairwise interaction and the contribution of the electron charge density from the nearest neighbors of the atom under consideration. In this study, we use the EAM potential of Zhakhovskii for aluminum [35]. This potential accurately describes triple point experimental data, reproduces mechanical and thermodynamical parameters at normal conditions, and gives a good agreement with the cold and Hugoniot curves [36]. Moreover, the phase equilibrium parameters for the liquid-gas and solid-liquid transitions [37] are determined and compared with the thermodynamic equation of state (EOS). A standard technique of a two-phase system equilibration is applied with both phases coexisting in the MD computational domain in mechanical, thermal, and chemical equilibrium. The results of these simulations together with the EOS phase diagram [38] are shown in Fig. 1 in density-temperature coordinates. One can observe a quite good agreement between the EOS and EAM binodal curves, and the difference is given by the binding of models to different parameters in the critical point (CP), which are not established precisely for the majority of metals. The CP parameters corresponding to the MD potential can be estimated as $T_{\rm CP} \approx 8$ kK and $\rho_{\rm CP} \approx 0.5$ g/cm^3 (see imaginary point of the MD binodal maximum in Fig. 1), whereas thermodynamic EOS parameters in the CP are $T_{\rm CP} = 6.6$ kK and $\rho_{\rm CP} = 0.7$ g/cm^3. The melting curve slope is steeper and wider for the EOS in comparison with the MD results.

A strong laser heating of the electron subsystem results in the appearance of energy transmission channel from the high-energy electrons to the atoms [22]. Thus, for each atom, we solve the equation of motion in the following form:

$$m_i \frac{d^2\mathbf{r}_i}{dt^2} = \mathbf{F}_i + \xi_i m_i \mathbf{v}_i^T. \tag{1}$$

Here, m_i is the mass of the ith atom, $\mathbf{r}_i$ is the radius-vector of the atom, t is the time, $\mathbf{F}_i$ is the force due to interaction of the ith atom with the surrounding atoms, ξ_i is the friction coefficient due to the absence of thermal equilibrium between electrons and ions [22], and $\mathbf{v}_i^T$ is the thermal velocity of the ith atom (the speed of the atom with respect to the center of mass of an elementary volume V, containing this atom). This elementary volume V (the numerical cell) is small enough compared with the target size, but still contains many atoms $N \gg 1$. As a result, the thermal velocity for the atom i can be expressed as

$$\mathbf{v}_i^T = \mathbf{v}_i - \mathbf{v}^c. \tag{2}$$

Here, $\mathbf{v}_i = \{u_i, v_i, w_i\}$ is the atom velocity and $\mathbf{v}^c = \{u^c, v^c, w^c\}$ is the speed of the center of mass of atoms inside the volume V, which can be calculated as follows:

$$\mathbf{v}^c = \sum_{i=1}^{N} (m_i \mathbf{v}_i) \Bigg/ \sum_{i=1}^{N} m_i. \tag{3}$$

Previously, an expression for the coefficient ξ_i was derived in Ref. [22] describing the rate of temperature relaxation between the electronic and ionic subsystems. First, we introduce the temperature of atoms inside the volume V as the mean kinetic energy per atom as follows:

$$T_{\rm ion} = \frac{1}{3k_B N} \sum_{i=1}^{N} m_i \left(\mathbf{v}_i^T\right)^2, \tag{4}$$

where k_B is the Boltzmann constant. Then, for all atoms belonging to the volume V, the coupling coefficient ξ_i is the same [22] and is given by

$$\xi_i \equiv \xi_V = \frac{\gamma V (T_{\rm el} - T_{\rm ion})}{\sum_{i=1}^{N} m_i \left(\mathbf{v}_i^T\right)^2} = \frac{\gamma V (T_{\rm el} - T_{\rm ion})}{3 k_B N T_{\rm ion}}, \tag{5}$$

where $T_{\rm el}$ is the electron temperature.

Note that the MD-TTM models [22,25,26,31] do not guarantee the conservation of the total energy of the system since the thermal conductivity equation for free electrons does not account of material motion. To remedy this shortcoming, we describe the evolution of the electron subsystem with the aid of continual energy equation in the Eulerian form as follows:

$$\frac{\partial(\rho e_{\rm el})}{\partial t} + \frac{\partial(\rho e_{\rm el} w)}{\partial z} = \frac{\partial}{\partial z}\left(\kappa \frac{\partial T_{\rm el}}{\partial z}\right) - \gamma (T_{\rm el} - T_{\rm ion}) + Q_L(t,z). \tag{6}$$

Here, ρ is the material density, z is the normal to the target surface coordinate, w is the velocity in the z direction ($w = w^c$), and $e_{\rm el}$ is the specific energy of free electrons. The energy exchange between electron and ion subsystems is described by the corresponding term with the coupling factor $\gamma(\rho, T_{\rm el}, T_{\rm ion})$ and the electron heat transfer is specified by the thermal conduction coefficient $\kappa(\rho, T_{\rm el}, T_{\rm ion})$. We use a standard operator splitting technique [39] for Eq. (6) to perform fractional time steps for different physical operators associated with the collective motion of atoms and microscopic processes inside the electron subsystem:

$$\frac{(\rho e_{\mathrm{el}})_j^* - (\rho e_{\mathrm{el}})_j^n}{\Delta t} + \frac{(\rho e_{\mathrm{el}} w)_{j+1/2}^n - (\rho e_{\mathrm{el}} w)_{j-1/2}^n}{\Delta z} = 0, \tag{7a}$$

$$\frac{(\rho e_{\mathrm{el}})_j^{n+1} - (\rho e_{\mathrm{el}})_j^*}{\Delta t} = \frac{\kappa_{j+1/2}^n \left(T_{\mathrm{el},j+1}^{n+1} - T_{\mathrm{el},j}^{n+1}\right)}{\Delta z^2} - \frac{\kappa_{j-1/2}^n \left(T_{\mathrm{el},j}^{n+1} - T_{\mathrm{el},j-1}^{n+1}\right)}{\Delta z^2} - \gamma_j^n \left(T_{\mathrm{el},j}^n - T_{\mathrm{ion},j}^n\right) + Q_{L,j}^n. \tag{7b}$$

Here, Δt is the time step ($t^{n+1} = t^n + \Delta t$) and Δz is the spatial discretization step ($z_{j+1} = z_j + \Delta z$). We suppose the full neutrality of the entire system in each volume of interest V_j and, thus, any atom and its bounded and free electrons move together so that Eq. (7a) is reformulated as follows:

$$N_j^* e_j^* = N_j^n e_j^n + N_{j-1/2}^+ e_{j-1}^n - N_{j-1/2}^- e_j^n - N_{j+1/2}^+ e_j^n + N_{j+1/2}^- e_{j+1}^n, \tag{8}$$

where N_j^* is the number of atoms in the cell j after the advection step, N_j^n is the initial number of atoms in the cell, $N_{j-1/2}^+$ is the number of atoms flowing into the cell j through the boundary $j - 1/2$ from the cell $j - 1$, and $N_{j-1/2}^-$ is the number of atoms flowing out of the cell j through the boundary $j - 1/2$ from the cell j. Similarly, $N_{j+1/2}^-$ and $N_{j+1/2}^+$ are the number of incoming and outgoing atoms through the boundary $j + 1/2$, respectively. An obvious equality is satisfied $N_j^* = N_j^n + N_{j-1/2}^+ - N_{j-1/2}^- - N_{j+1/2}^+ + N_{j+1/2}^-$ at each time step, so that the electron energy conservation associated with material motion is achieved due to Eq. (7a). Note that we apply an implicit scheme to advance in time the heat conductivity term in Eq. (7b) and avoid numerical instabilities when the magnitude of the electron thermal conductivity coefficient is high. For an explicit scheme in this case, one needs to apply a series of substeps [22] to meet the Courant-Friedrichs-Lewy condition of stability.

The laser energy absorption by the CB (in condensed phase) or free (in plasma) electrons is taken into account with the aid of the heat source term $Q_L(t,z)$. For its calculation, we solve numerically the Helmholtz wave equation for the electric field envelope with proper boundary conditions [40] and normal incidence of the beam:

$$\frac{\partial^2 E}{\partial z^2} + \frac{\omega_L^2}{c^2}\varepsilon(z)E = 0. \tag{9}$$

Here, E is the laser electric field envelope, ω_L is the laser frequency, and c is the speed of light, $\varepsilon(\omega_L,\rho,T_{\mathrm{el}},T_{\mathrm{ion}})$ is the high-frequency dielectric function. The resulting laser heating source is

$$Q_L(t,z) = \frac{\omega_L}{8\pi}\mathrm{Im}[\varepsilon(t,z)]|E(t,z)|^2.$$

The incident laser field amplitude is $E_L(t) = \sqrt{8\pi I(t)/c}$, where $I(t)$ is the incident laser intensity. Solution to the Eq. (9) is calculated using a transfer-matrix method [40]. Wide-range models of thermal conductivity κ, dielectric function ε and electron-ion coupling γ are used as described elsewhere [33]. The thermodynamic properties of electron subsystem are described by the thermal part of the Thomas-Fermi model [41] that gives the relations for the specific electron energy $e_{\mathrm{el}}(\rho,T_{\mathrm{el}})$ and the mean charge of ions, $Z(\rho,T_{\mathrm{el}})$ used for completeness of Eq. (6) and calculation of electron concentration $n_{\mathrm{el}} = Zn_{\mathrm{ion}}$. The temperature T_{el} at given ρ and e_{el} is obtained by an inverse transformation of the interpolation dependence $e_{\mathrm{el}}(\rho,T_{\mathrm{el}})$.

III. SIMULATION RESULTS AND DISCUSSION

In this study, we use parameters of Ti:sapphire laser setup with the wavelength 800 nm, the pulse duration $\tau = 100$ fs and the incident laser fluence $F_{\mathrm{inc}} = 2$ J/cm^2 for each pulse. The intensity time profile of the two succeeding pulses has the Gaussian form

$$I(t) = I_0 \exp[-\ln(16)t^2/\tau^2] + I_0 \exp[-\ln(16)(t - \tau_D)^2/\tau^2]$$

with a peak intensity $I_0 = 1.88 \times 10^{13}$ W/cm^2 that corresponds to the incident fluence of 2 J/cm^2, and the delay between pulses τ_D varies from 0 to 200 ps.

Initially, the target free surface is located at position $z = 0$ nm and the laser beam propagation is in the positive direction of z. The thickness of the target in the MD simulation is 4 μm while the cross section is about 8×8 nm (20×20 periods of the fcc aluminum crystal). The chosen target thickness of 4 μm is sufficient to investigate the initial stage of the front laser ablation up to 1000 ps until the waves reflected from the back free surface reach the heat affected zone. The total number of atoms in a typical run is 1.58×10^7. The MD part of the code is based on the large-scale atomic/molecular massively parallel simulator (LAMMPS) [42]. For calculation of macroscopic characteristics, an averaging of atomic data is performed over the $8 \times 8 \times 2$ nm volumes (the mesh size in the z direction is 2 nm and the initial number of atoms in this volume is about 1.6×10^4).

Figure 2 shows the localization of the second pulse laser energy absorption for different delays τ_D between pulses. When $\tau_D = 0$ ps, the dynamics of ablation corresponds to an SP case with an incident fluence of 4 J/cm^2. The laser energy absorption by the CB electrons occurs in the skin layer of about 30-nm thickness. Then, for 10 and 20 ps delays, one can observe the shift and enlargement of the second

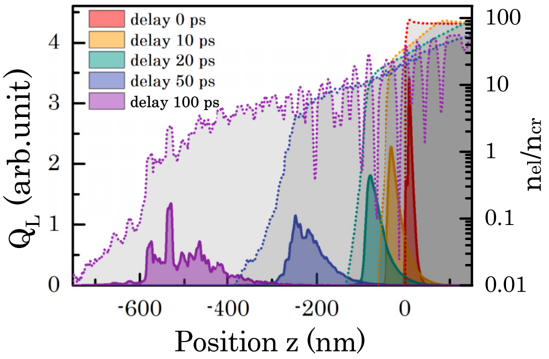

FIG. 2. (Color online) Localization of the second pulse absorption and normalized concentration of electrons for different delays between pulses.

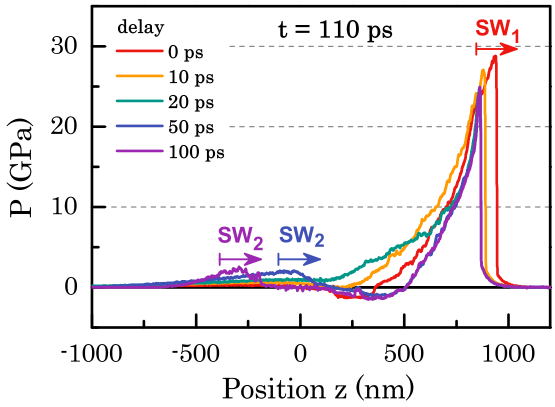

FIG. 3. (Color online) Pressure distribution in the target at the moment $t = 110$ ps for different delays between pulses.

pulse absorption region as the target material rarefaction starts after the first pulse action. For these delays, the target interfaces at the moment of the second pulse arrival are located at a distance of about 50 and 100 nm from the initial free surface position, respectively. Note that the second pulse absorption for the delays $\lesssim$20 ps corresponds to a supercritical regime ($n_{\rm el}/n_{\rm cr} \gtrsim 10$), and is qualitatively close to the Beer's law. Here, $n_{\rm cr} = \omega_L^2 m_e/(4\pi e^2)$, and m_e and e are the electron mass and charge, respectively. For longer delays, we observe further target expansion and localization of the second pulse absorption is at $-300 \lesssim z \lesssim -100$ nm and $-600 \lesssim z \lesssim -300$ nm for 50 and 100 ps delays, respectively. For these delays, the nascent plasma plume completely shields the target surface from the action of the second pulse similar to the results of experimental findings [1]. As one can see, the laser energy absorption on such nonmonotonic space profiles of free electron concentration requires a solution of the wave equation. As a result of different space localization and efficiency of the second pulse absorption, the dynamics of the target ablation varies with the delay.

The evolution of heated substance for different delays can be considered in terms of pressure waves that are shown in Fig. 3. For the delay of 0 ps, only one shock wave (SW$_1$) is generated with the amplitude of about 30 GPa at the moment 110 ps (see Fig. 3). When the delay increases, the amplitude of the SW$_1$ drops to 25 GPa (for 100 ps delay case). At the same time, the negative pressure region associated with the strong rarefaction wave (RW), that is, the reason of material fragmentation disappears for the delays from 10 to 20 ps. The observed suppression of the RW is the cause of the crater depth reduction for short delays between pulses observed in experiment. Instead, for longer delays $\gtrsim$50 ps, one can see the formation of the second SW (SW$_2$) generated by the second pulse in the nascent plasma plume. As we show later, the formation of this SW$_2$ will lead to a further reduction in the ablation crater depth.

Ablation dynamics is analyzed by using contour plots of the main thermodynamic parameters in the target for different delays between pulses. The case of 0 ps delay is presented in Fig. 4 for the density, temperature of atoms, and pressure. For this delay, the laser energy absorption occurs in a skin layer of about 30 nm and the temperature of CB electrons increases during the pulse up to 75 kK. The electron thermal conductivity results in a steep electron temperature gradient smearing; the transition of electron energy to the lattice initiates a homogeneous melting of the target and at the moment of $t \approx 100$ ps the melted depth reaches 350 nm [see Fig. 4(a)]. The SW travels inside the bulk at a speed of 8 km/s. The length of the plasma plume at this time is about 1 μm and the temperature of atoms (the electron temperature is close to the atomic one due to relaxation by this time) reaches 15 kK [Fig. 4(b)], which corresponds to a supercritical state [the temperature in the CP for the used potential is about 8 kK (see Fig. 1)]. The RW [the blue region in Fig. 4(c)] succeeds the SW (the red and black regions) and initiates the nucleation process in a liquid layer, so that in the interval of 100–150 ps the formation of ablated layers is completed [see Fig. 4(a)].

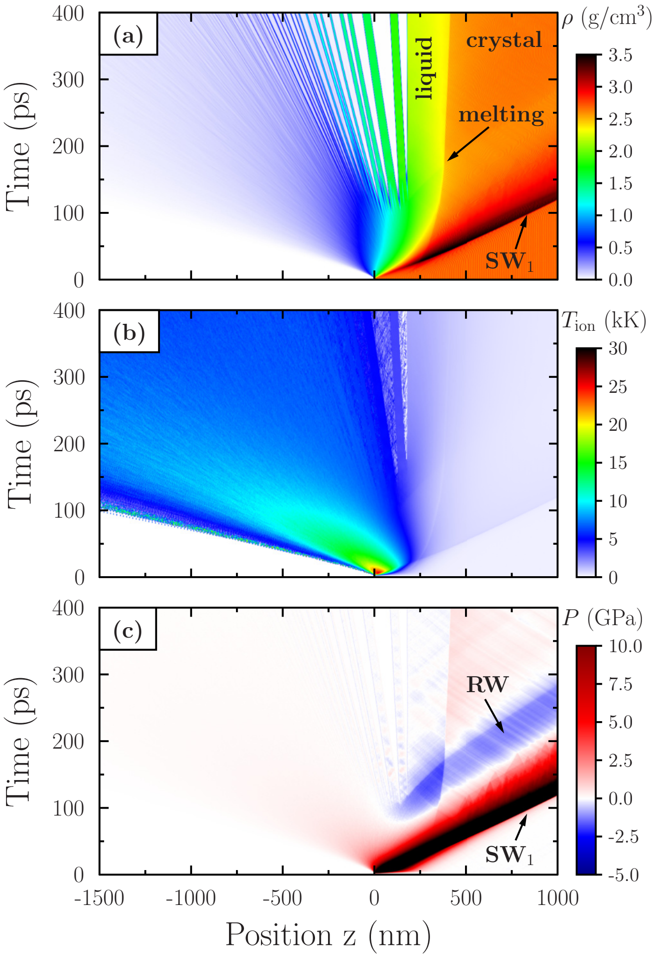

FIG. 4. (Color online) Contour plots of the density (a), temperature of ions (b), and pressure (c) for 0 ps delay between pulses.

The ablation dynamics changes when the delay between pulses reaches 10 ps. As one can see, in Fig. 5(a) in this case, the moment of liquid layer spallation occurs later (at $t \approx 150$ ps). The temperature in the plume is higher and reaches 30 kK, while the plume length also increases up to 1.5 μm at the moment of 100 ps in comparison with 0 ps delay [compare Figs. 4(b) and 5(b)]. One can also observe the decrease of the ablation layer thickness while the melted depth remains the same [compare Figs. 4(a) and 5(a)]. For a longer delay of 20 ps, we observe a subsequent decrease in the fragmentation dynamics that starts now at about 200 ps [Fig. 6(a)]. The

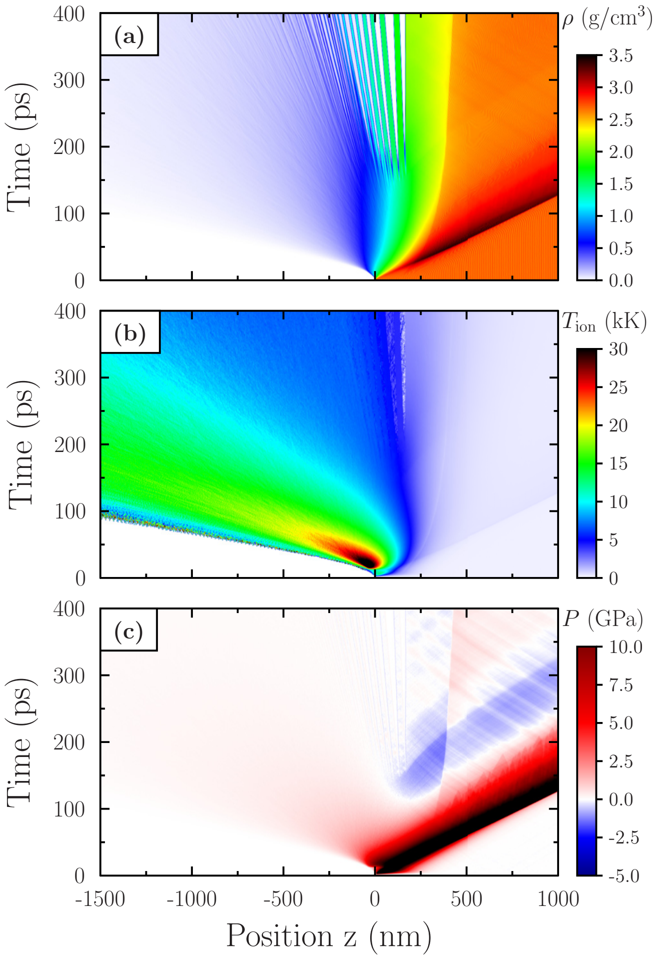

FIG. 5. (Color online) The same as in Fig. 4 but for 10 ps delay between pulses.

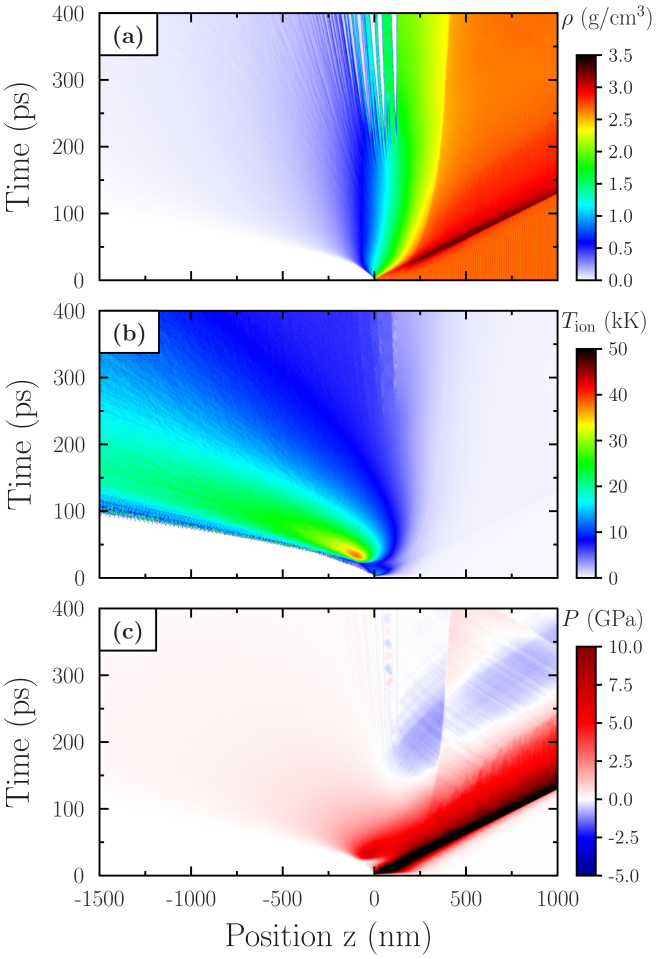

FIG. 6. (Color online) The same as in Fig. 4 but for 20 ps delay between pulses.

pressure wave is split into two waves as one can see in Fig. 6(c). The zone of the second pulse absorption is also clearly seen at $-100 \lesssim z \lesssim 0$ nm in Fig. 2. This extension of the absorption region is the reason of the formation of a weaker RW. As a result, the fragmentation intensity lessens and ablation mass drops but the melted layer remains similar to 0 ps delay case.

When the delay between pulses is increased to 50 ps, the second mechanism of suppression of laser-induced ablation appears. As one can see in Fig. 2, the second pulse is absorbed within the range of $-300 \lesssim z \lesssim -100$ nm and at this moment the RW (produced by the first pulse) passes through the melted surface layer and causes fragmentation in it, [see panels (a) and (c) in Fig. 7 at $t \approx 50$ ps]. The plasma temperature reaches the value of 50 kK in the zone of the second pulse energy absorption. The second SW forms in this region, travels through the ablated layers and causes the collapse of the nascent voids between nano-layers. These layers get in contact with the target, and the process of condensation and recoil from the plume occurs at $t \gtrsim 400$ ps [see Fig. 7(a)]. The pressure wave with amplitude of about 2 GPa starts its motion from the plume region into the bulk of the target. This wave is followed by the second RW but its intensity is not sufficient to cause spallation of the liquid layer. Note, that the thickness of the melted region is bigger and reaches 450 nm for this delay [see Fig. 7(a)].

For the delay of 100 ps, we observe the second pulse energy absorption at $z \approx -500$ nm when the temperature of atoms in the plume reaches the maximum value of 70 kK [see Fig. 8(b)]. The deceleration of matter between the zone of absorption and the target is clearly seen at $100 \lesssim t \lesssim 350$ ps in Fig. 8(a). The intensity of the second SW (SW_2) is sufficient to completely eliminate the fragmentation produced by the first pulse [see Figs. 8(a) and 8(c)]. As the absorption of the second pulse takes place far enough from the initial surface of the target (in the leading edge of the nascent ablation plume) it takes time to cause the collapse of voids and this process is finished at the moment $t \approx 350$ ps. An extra melting of the target is also observed starting from this event, since the attached layers are heated above the melting temperature [compare melted layer thickness in Fig. 8(a) at 350 and 1000 ps].

We can follow in more detail the dynamics of ablation with the aid of MD snapshots presented in Fig. 9 for the case of 100 ps delay. As one can see in Fig. 9(a), at $t = 7$ ps, the high-pressure region $0 \lesssim z \lesssim 150$ nm is formed in the target by the first pulse and the motionless region with z component of the drift speed $w \approx 0$ is located at about 40 nm depth (atoms colored in white). This 40 nm depth corresponds to the pressure maximum at this moment. The deeper atoms have a drift velocity of the order of 1 km/s (atoms colored in shades

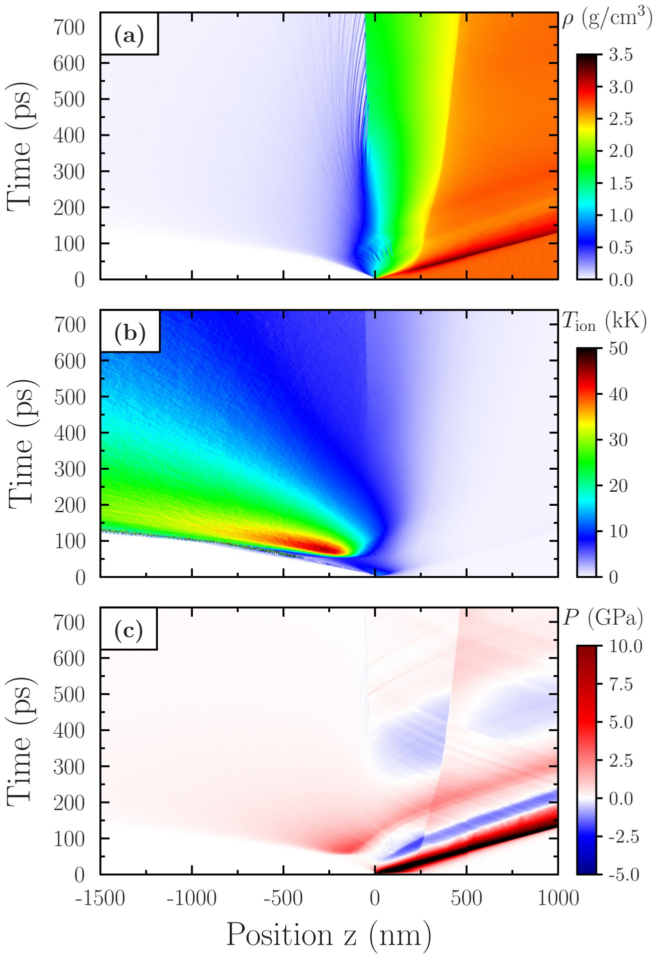

FIG. 7. (Color online) The same as in Fig. 4 but for 50 ps delay between pulses.

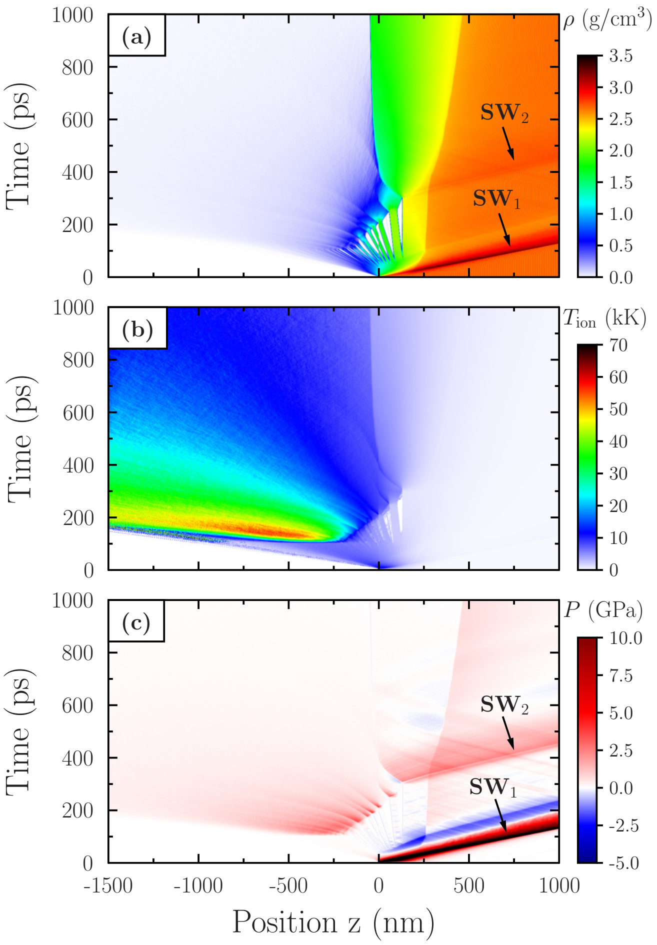

FIG. 8. (Color online) The same as in Fig. 4 but for 100 ps delay between pulses.

of red) corresponding to the initial stage of the SW formation while the atoms close to the free surface $z \lesssim 40$ nm move out at a speed of about -3 km/s (atoms colored in shades of blue) forming the RW (first 25 nm of matter propagates at faster speed of $w \approx -5$ km/s). In Fig. 9(b), we see the rarefaction regime when the region $-300 \lesssim z \lesssim 200$ nm moves out of the bulk of the target and the minimum of pressure is achieved at $z \approx 100$ nm. At this moment, the pressure relaxation is completed in the considered region and its amplitude is below 1 GPa. The next snapshot ($t = 93$ ps) is close to the moment of the second pulse arrival (100 ps), and the laser pulse interaction with the smeared density profile goes more effectively in comparison with the first pulse interacting with the bulk target at normal conditions. It is also seen in panel (c), the formation of voids inside the melted stretched region $-300 \lesssim z \lesssim 150$ as a result of strong RW propagation. The maximum of the second pulse absorption is located at a distance of about 500 nm from the initial free surface [see temperature rise in Fig. 8(b) at $t \approx 100$ ps]. This high-pressure zone produces a secondary RW and SW. The propagation of the secondary SW at the moment of $t = 129$ ps is seen in panel (d) and the SW front is localized at $z \approx -200$ nm. This panel shows the initial stage of the void collapse under the action of SW$_2$. As the matter gets additional momentum in the positive direction of z due to SW$_2$, one can see in Fig. 8(e) the deceleration of atoms, and two groups of atoms having the positive drift speed at $z \approx -170$ nm and $z \approx -70$ nm. The SW propagation towards the target eventually generates a lengthy region of atoms that move in the positive direction of z at $w \approx 1$ km/s resulting in the collapse of voids [see Figs. 9(f) and 9(g)]. Then, at $t = 303$ ps the SW reaches $z \approx 150$ nm and the voids produced by the first pulse disappear [see Fig. 9(h)]. Finally, after thermal and mechanical relaxations, we observe the formation of a new target surface at $z \approx -50$ nm while the process of deposition of atoms is still in progress at this moment [see atoms colored in red in Fig. 9(i)]. As one can see, the condensation process continues till 1000 ps when the initial stage of the crater formation is finished [see Fig 8(a)].

Finally, for the longest delay of 200 ps in our simulation, the laser energy of the second pulse is absorbed in the plume at $-1300 \lesssim z \lesssim -700$ nm. The origin of the SW takes place in this region and the motion of this wave is clearly seen in Fig. 10(a). The speed of this disturbance in the time interval from 200 to 500 ps is about 1.7 km/s and the subsequent layer by layer reheating of matter results in disintegration of all liquid layers. Eventually, at 500 ps the plume configuration consists of a hot supercritical phase at $T_{\rm ion} \approx T_{\rm el} \gtrsim 10$ kK. The merging of the plume with the target liquid layer of thickness $\approx$150 nm occurs at 500 ps [see Fig. 10(a)]. The heterogeneous melting is observed till the moment of 1100 ps and the melted

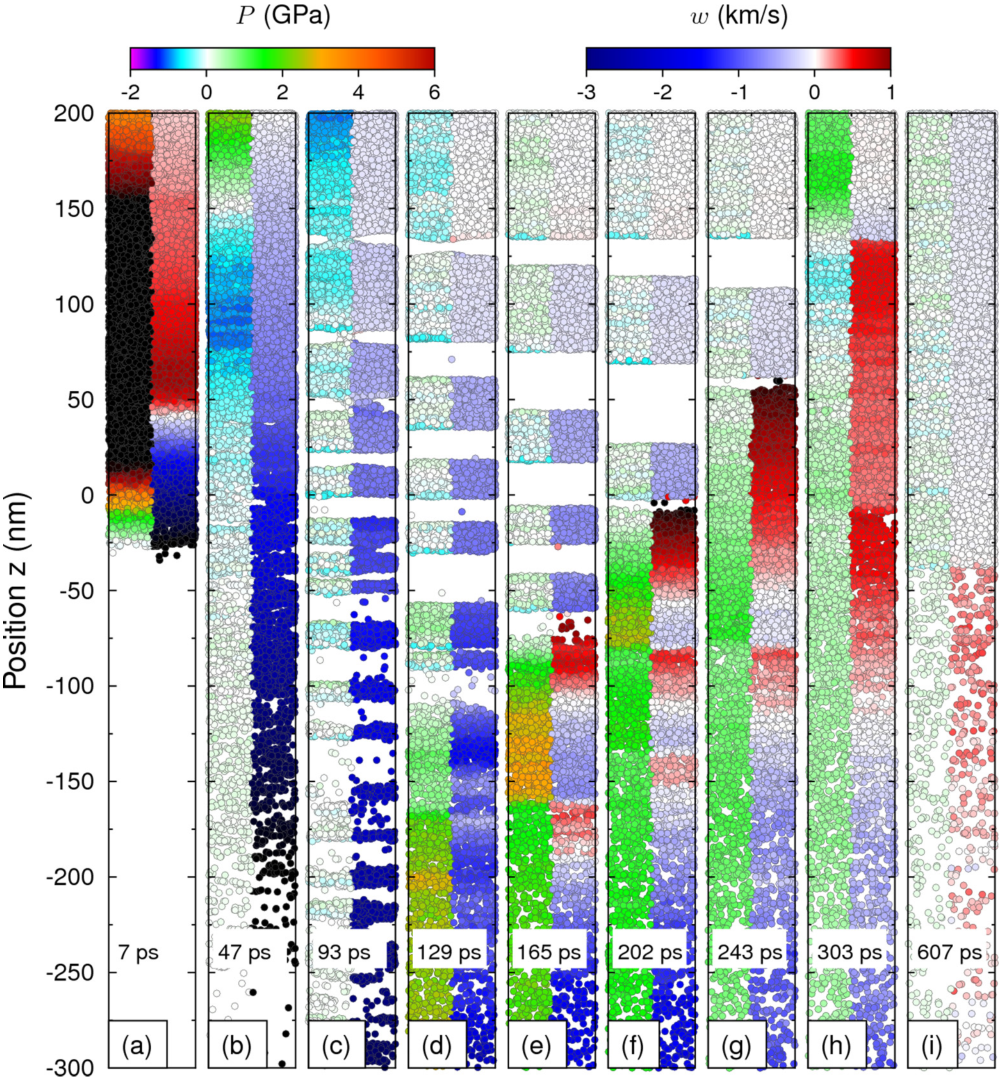

FIG. 9. (Color) MD snapshots for 100 ps delay between pulses: (a) 7, (b) 47, (c) 93, (d) 129, (e) 165, (f) 202, (g) 243, (h) 303, and (i) 607 ps. Atoms in the left half of panels are colored according to the pressure value; atoms in the right half of panels are colored according to their hydrodynamic (drift) speed w in z direction.

depth reaches about 450 nm by this instant. As in the case of 100 ps delay, the processes of the target melting and deposition of atoms from the gas phase are still goes on, but the new surface is already formed.

Thereby, we can conclude that two mechanisms are responsible for the suppression of ablation in the DP irradiation of metallic targets. The first one is associated with the suppression of the RW responsible for the process of homogeneous nucleation in the liquid layer of the target under the action of tensile stress. This mechanism dominates for delays $\tau_D \lesssim$ 20 ps and results in the monotonic decrease of the crater depth. For delays longer than 50 ps, there is enough time for the mechanical fragmentation to occur under the action of the first pulse, but the second pulse produces a high-pressure plasma ahead of the ablated liquid layers and pushes the large fraction of these ablated layers back to the target. In this case, the ablation depth is even smaller than that in the case of a SP. Note, that the second mechanism can also initiate the splash effect on later times that is not resolved in the frame of our quasi-one-dimensional model.

The dynamics of plasma reheating is essential for the increase of spectral lines intensities in LIBS technique. Figure 11 shows the dependence of the integral absorption of the second pulse by the nascent plasma plume as a function of delay. It is clearly seen that the absorbed fluence grows from 25% to 98% when the delay varies from 0 to 200 ps. The reason is that the electron density profile becomes more gradual, and the second pulse absorption region widens with the increasing delay (see Fig. 2). As a result of a more effective absorption, one can expect the growth of maximum temperature with the delay. In Fig. 12, we present the maximum temperature of electrons, that is reached immediately after the second pulse action (empty red circles). The temperature of electrons 100 ps after the second pulse action (filled blue circles) is also shown in Fig. 12, demonstrating almost a three-fold growth of electron temperature in the plume as the delay changes from 0 to 200 ps. Attempts to simulate the longer delays face serious computational difficulties. Indeed, our results show that the second pulse absorption for the delays of about 200 ps occurs already at ~1 μm before the target surface [see Fig. 10(b)].

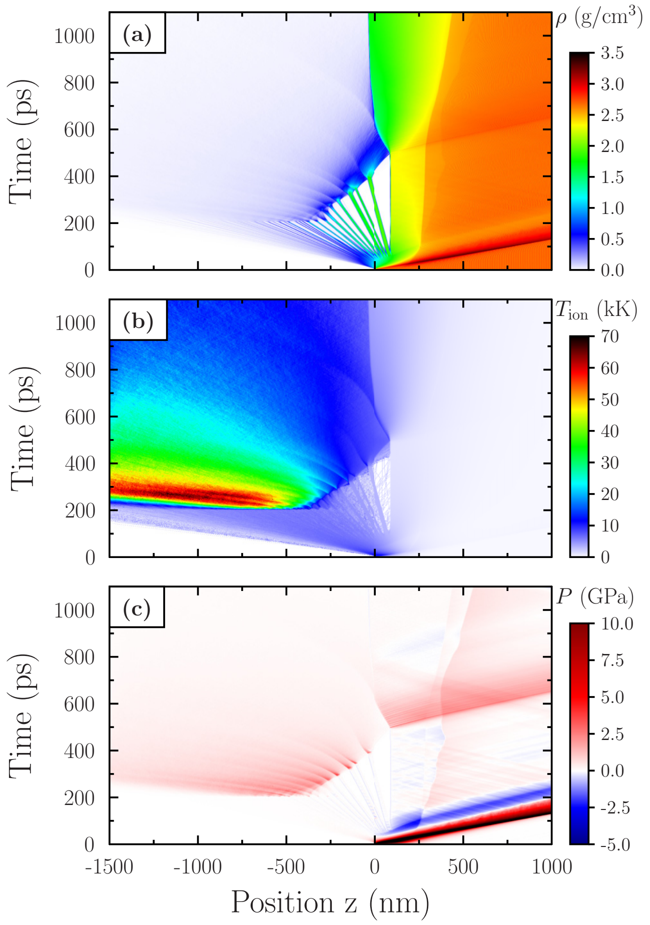

FIG. 10. (Color online) The same as in Fig. 4 but for 200 ps delay between pulses.

This characteristic length of the plume is comparable to the typical laser spot diameter, and, thus, effects of a strong rarefaction in the transversal direction start to play a significant role. As a result, one can expect a faster decrease of the electron density during the expansion in comparison with our 1D analysis. When the electron concentration drops significantly below the critical value n_{cr}, the second pulse can interact directly with the solid target. Moreover, the thick ablated layers in the liquid phase can undergo the fragmentation into a 3D cloud of droplets that is also more transparent to the second pulse. All these processes might be properly described with the aid of new 3D models, which require considerable computational resources.

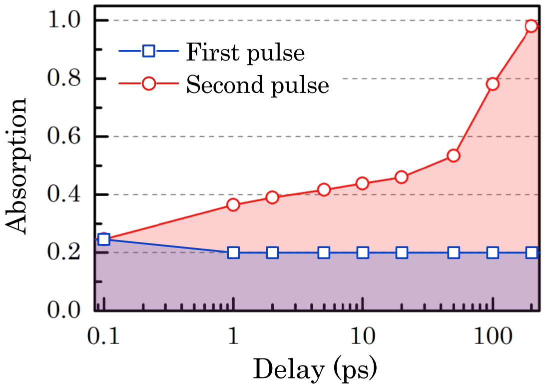

FIG. 11. (Color online) Integral absorption of the first (empty blue squares) and the second (empty red circles) pulses as a function of the delay between them. The fluence of each pulse is 2 J/cm^2.

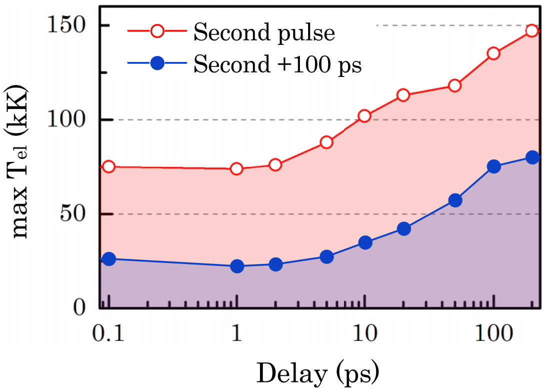

FIG. 12. (Color online) The electron temperature maximum [empty (red) circles] and the electron temperature 100 ps after the second pulse [filled (blue) circles].

To remedy the lack of information for very long delays between pulses, we perform additional estimations of the plume dynamics produced by the first pulse using a 1D two-temperature hydrodynamic (HD) model [33]. Results of the HD modeling demonstrate that for the delays $\gtrsim$1 ns the liquid-gas mixture in front of the plume is already transparent for the second pulse, and the beam interacts with the liquid droplets forming the tail of the plume. Thereby, one could expect the decrease of the second pulse absorption in the plume and the subsequent plume temperature lessening for the delays $\gtrsim$1 ns. For even longer delays, we conjecture the tendency of the second pulse dynamics to the SP case.

Figure 13 shows the ablation depth as a function of fluence. The case with 0 ps delay is identical to a SP with the fluence $2 \times F_{\mathrm{inc}} = 4$ J/cm^2. Then, as the delay increases, the ablation

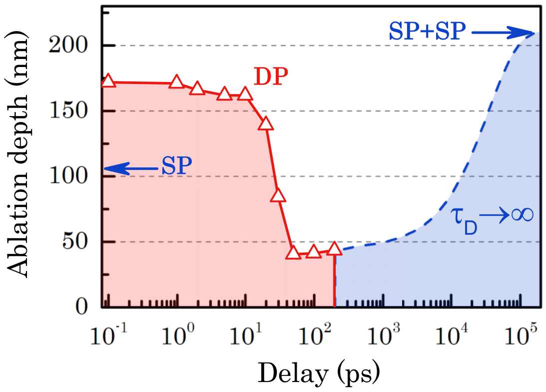

FIG. 13. (Color online) Ablation depth dependence on the delay between two succeeding pulses with fluence 2 J/cm^2 each [empty (red) triangles]. Extrapolation to very long delays is shown by dashed (blue) curve. Blue arrows show the ablation depth of a SP with fluence 2 J/cm^2 and two succeeding SPs with the delay $\tau_D \to \infty$.

depth starts to drop and by the delay of about 30 ps it reaches the SP ablation depth with the fluence F_{inc}. For longer delays, the ablation depth monotonically reaches the value below the SP level that is also observed in experiment [1,5]. Note that we explicitly calculate the number of atoms escaped from the target and, thus, find out the ablation depth (the precipitation flux is taken into account automatically). We can also extrapolate the ablation depth for very long delays unachievable in simulation (see dashed blue curve in Fig. 13). Indeed, the plasma plume produced by the first pulse expands and eventually reaches a subcritical electron density. For this moment, the transmission of the plume starts to grow and the second pulse again reaches the target enlarging the ablation crater depth. Experimentally observed linear growth of the crater depth with the number of pulses [1,43] supports the final value of extrapolated depth at $t_D \to \infty$ as the twofold depth of the SP. Our model is quasi-1D and does not take into account transversal effects such as laser intensity distribution within the spot, nonhomogeneous plume expansion, and surface waves. Besides, our calculations are limited by 1 ns time and DP delays of about 200 ps. In experiments, the role of 3D effects in the formation of a crater is very important and the final shape and depth of the crater depends on recrystallization, expulsion of the melted substance from the central zone, and thermocapillary effects [44]. All these processes are out of the scope of this paper.

IV. CONCLUSIONS

We have developed the MD-TTM approach for simulation of laser ablation of metals. Laser energy absorption, electron thermal conductivity, and electron-phonon/ion coupling are taken into account by means of wide-range models of optical and transport coefficients. To correctly describe the laser energy absorption, the Helmholtz wave equation is solved giving the possibility to deal with arbitrary profiles of electron density and temperature. We use an accurate EAM potential, the phase diagram of which agrees well with the one known from experiment. It has been demonstrated in the set of simulations of DP ablation of aluminum that the reheating of plasma reaches a maximum at delays $\gtrsim$100 ps when the absorption of the second pulse changes from 25% at 0 ps delay to 98% at 200 ps delay. For delays $\gtrsim$20 ps, the plasma shielding effect is observed and the second pulse does not reach the target. This result is close to the one observed in experiments [1,4]. Also, for a 100–200 ps delay, we observe a three-fold growth of the plume temperature that explains the increase of the luminosity of the plume recorded in the experiments. The crater depth reduction observed both in the experiments and the presented modeling is due to the formation of a high-pressure zone inside the plume that suppresses the fragmentation in RW caused by the first pulse for delays $\lesssim$20 ps, and merges the inner ablated layers of atoms with the target surface for delays $\gtrsim$50 ps. The obtained results can be used in further development of such applications as LIBS and matrix-assisted laser desorption/ionization, as well as in laser nanostructuring of surfaces and in medical applications.

ACKNOWLEDGMENTS

The authors thank V. Zhakhovskii for the data on two-phase MD modeling and valuable discussions. This work was supported by the Russian Foundation for Basic Research (Project Nos. 13-08-01179 and 13-02-91057), Presidium of RAS program “Fundamental problems of numerical simulation”, and by France-Russia collaborative project PICS 6106 of DRI/CNRS.

---

[1] A. Semerok and C. Dutouquet, Thin Solid Films **453-454**, 501 (2004).
[2] D. Scuderi, O. Albert, D. Moreau, P. P. Pronko, and J. Etchepare, Appl. Phys. Lett. **86**, 071502 (2005).
[3] V. Piñon, C. Fotakis, G. Nicolas, and D. Anglos, Spectrochimica Acta Part B **63**, 1006 (2008).
[4] J. Mildner, C. Sarpe, N. Götte, M. Wollenhaupt, and T. Baumert, Appl. Surf. Sci. **302**, 291 (2014).
[5] T. Donnelly, J. G. Lunney, S. Amoruso, R. Bruzzese, X. Wang, and X. Ni, J. Appl. Phys. **106**, 013304 (2009).
[6] S. Noël and J. Hermann, Appl. Phys. Lett. **94**, 053120 (2009).
[7] E. Loktionov, A. Ovchinnikov, Y. Protasov, Y. Protasov, and D. Sitnikov, High Temp. **52**, 132 (2014).
[8] H. Muto, K. Miyajima, and F. Mafuné, J. Phys. Chem. C **112**, 5810 (2008).
[9] V. Karpukhin, M. Malikov, T. Borodina, G. Val’yano, O. Gololobova, and D. Strikanov, High Temp. **53**, 93 (2015).
[10] M. Rohloff, S. Das, S. Höhm, R. Grunwald, A. Rosenfeld, J. Krüger, and J. Bonse, J. Appl. Phys. **110**, 014910 (2011).
[11] T. J.-Y. Derrien, J. Krüger, T. E. Itina, S. Höhm, A. Rosenfeld, and J. Bonse, Appl. Phys. A **117**, 77 (2014).
[12] Y. Cherednikov, N. A. Inogamov, and H. M. Urbassek, Phys. Rev. B **88**, 134109 (2013).
[13] C. Wu, M. S. Christensen, J.-M. Savolainen, P. Balling, and L. V. Zhigilei, Phys. Rev. B **91**, 035413 (2015).
[14] G. Baffou and H. Rigneault, Phys. Rev. B **84**, 035415 (2011).
[15] R. A. Ganeev, C. Hutchison, I. Lopez-Quintas, F. McGrath, D. Y. Lei, M. Castillejo, and J. P. Marangos, Phys. Rev. A **88**, 033803 (2013).
[16] J. P. Colombier, P. Combis, E. Audouard, and R. Stoian, New J. Phys. **14**, 013039 (2012).
[17] J. P. Colombier, P. Combis, F. Bonneau, R. Le Harzic, and E. Audouard, Phys. Rev. B **71**, 165406 (2005).
[18] B. Chimier, V. T. Tikhonchuk, and L. Hallo, Phys. Rev. B **75**, 195124 (2007).
[19] M. E. Povarnitsyn, T. E. Itina, K. V. Khishchenko, and P. R. Levashov, Phys. Rev. Lett. **103**, 195002 (2009).
[20] M. E. Povarnitsyn, T. E. Itina, P. R. Levashov, and K. V. Khishchenko, Appl. Surf. Sci. **257**, 5168 (2011).
[21] C. Schäfer, H. M. Urbassek, and L. V. Zhigilei, Phys. Rev. B **66**, 115404 (2002).
[22] D. S. Ivanov and L. V. Zhigilei, Phys. Rev. B **68**, 064114 (2003).

[23] D. Perez and L. J. Lewis, Phys. Rev. B **67**, 184102 (2003).

[24] G. Norman, S. Starikov, V. Stegailov, V. Fortov, I. Skobelev, T. Pikuz, A. Faenov, S. Tamotsu, Y. Kato, M. Ishino, M. Tanaka, N. Hasegawa, M. Nishikino, T. Ohba, T. Kaihori, Y. Ochi, T. Imazono, Y. Fukuda, M. Kando, and T. Kawachi, J. Appl. Phys. **112**, 013104 (2012).

[25] S. V. Starikov and V. V. Pisarev, J. Appl. Phys. **117**, 135901 (2015).

[26] J. Roth, A. Krauß, J. Lotze, and H.-R. Trebin, Appl. Phys. A **117**, 2207 (2014).

[27] D. Perez, L. K. Béland, D. Deryng, L. J. Lewis, and M. Meunier, Phys. Rev. B **77**, 014108 (2008).

[28] M. Kaganov, I. Lifshitz, and L. Tanatarov, Zh. Eksp. Teor. Fiz. **31**, 232 (1956) [Sov. Phys. JEPT **4**, 173 (1957)].

[29] S. I. Anisimov, B. L. Kapeliovich, and T. L. Perel'man, Zh. Eksp. Teor. Fiz. **66**, 776 (1974) [Sov. Phys. JETP **39**, 375 (1974)].

[30] S. V. Starikov, V. V. Stegailov, G. E. Norman, V. E. Fortov, M. Ishino, M. Tanaka, N. Hasegawa, M. Nishikino, T. Ohba, T. Kaihori, E. Ochi, T. Imazono, T. Kavachi, S. Tamotsu, T. A. Pikuz, I. Y. Skobelev, and A. Y. Faenov, JETP Lett. **93**, 642 (2011).

[31] Y. Gan and J. K. Chen, Appl. Phys. Lett. **94**, 201116 (2009).

[32] S. V. Starikov, A. Y. Faenov, T. A. Pikuz, I. Y. Skobelev, V. E. Fortov, S. Tamotsu, M. Ishino, M. Tanaka, N. Hasegawa, M. Nishikino, T. Kaihori, T. Imazono, M. Kando, and T. Kawachi, Appl. Phys. B—Las. Opt. **116**, 1005 (2014).

[33] M. E. Povarnitsyn, N. E. Andreev, E. M. Apfelbaum, T. E. Itina, K. V. Khishchenko, O. F. Kostenko, P. R. Levashov, and M. E. Veysman, Appl. Surf. Sci. **258**, 9480 (2012).

[34] M. S. Daw and M. I. Baskes, Phys. Rev. B **29**, 6443 (1984).

[35] V. Zhakhovskii, N. Inogamov, Y. Petrov, S. Ashitkov, and K. Nishihara, Appl. Surf. Sci. **255**, 9592 (2009).

[36] *High-Pressure Shock Compression of Solids*, edited by J. R. Asay and M. Shahinpoor (Springer-Verlag, New York, 1993) p. 399.

[37] V. V. Zhakhovskii (private communication).

[38] M. E. Povarnitsyn, T. E. Itina, M. Sentis, K. V. Khishchenko, and P. R. Levashov, Phys. Rev. B **75**, 235414 (2007).

[39] D. Lanser and J. Verwer, J. Comp. Appl. Math. **111**, 201 (1999).

[40] M. E. Povarnitsyn, N. E. Andreev, P. R. Levashov, K. V. Khishchenko, and O. N. Rosmej, Phys. Plasmas **19**, 023110 (2012).

[41] O. P. Shemyakin, P. R. Levashov, L. R. Obruchkova, and K. V. Khishchenko, J. Phys. A: Math. Theor. **43**, 335003 (2010).

[42] S. Plimpton, J. Comput. Phys. **117**, 1 (1995).

[43] J. Hermann, S. Noël, T. E. Itina, E. Axente, and M. E. Povarnitsyn, Laser Phys. **18**, 374 (2008).

[44] V. S. Ajaev and D. A. Willis, Phys. Fluids **15**, 3144 (2003).